UCRL-JRNL-203825

LAWRENCE
LIVERMORE
NATIONAL
LABORATORY

# Evidence for the predominance of mid-tropopheric aerosols as subtropical anvil nuclei

Ann Fridland, Andy Ackermann, Eric Jensen, David Stevens

April 28, 2004

Science

**Disclaimer**

This document was prepared as an account of work sponsored by an agency of the United States Government. Neither the United States Government nor the University of California nor any of their employees, makes any warranty, express or implied, or assumes any legal liability or responsibility for the accuracy, completeness, or usefulness of any information, apparatus, product, or process disclosed, or represents that its use would not infringe privately owned rights. Reference herein to any specific commercial product, process, or service by trade name, trademark, manufacturer, or otherwise, does not necessarily constitute or imply its endorsement, recommendation, or favoring by the United States Government or the University of California. The views and opinions of authors expressed herein do not necessarily state or reflect those of the United States Government or the University of California, and shall not be used for advertising or product endorsement purposes.

This work was performed under the auspices of the U.S. Department of Energy by the University of California, Lawrence Livermore National Laboratory under Contract No. W-7405-Eng-48.

# Evidence for the predominance of mid-tropospheric aerosols as subtropical anvil nuclei

Ann M. Fridlind,[1*] Andrew S. Ackerman,[1] Eric J. Jensen,[1]
Andrew J. Heymsfield,[2] Michael R. Poellot,[3] David E. Stevens,[4]
Donghai Wang,[5] Larry M. Miloshevich,[2] Darrel Baumgardner,[6]
R. Paul Lawson,[7] James C. Wilson,[8] Richard C. Flagan,[9]
John H. Seinfeld,[9] Haflidi H. Jonsson,[10] Timothy M. VanReken,[9]
Varuntida Varutbangkul,[9] Tracey A. Rissman[9]

[1]NASA Ames Research Center, Moffett Field, CA 94035, USA
[2]National Center for Atmospheric Research, Boulder, CO 80307, USA
[3]University of North Dakota, Grand Forks, ND 58202, USA
[4]Lawrence Livermore National Laboratory, Livermore, CA 94552, USA
[5]Hampton University and NASA Langley Research Center, Hampton, VA 23681, USA
[6]Universidad Nacional Autonoma de Mexico, Mexico City, MEX
[7]SPEC Inc., Boulder, CO 80301, USA
[8]University of Denver, Denver, CO 80208, USA
[9]California Institute of Technology, Pasadena, CA 91125, USA
[10]Center for Interdisciplinary Remotely-Piloted Aircraft Studies, Marina, CA 93933, USA

*To whom correspondence should be addressed; E-mail: ann.fridlind@nasa.gov.

**NASA's recent CRYSTAL–FACE field experiment focused on anvil cirrus clouds, an important but poorly understood element of our climate system. Data obtained include the first comprehensive measurements of aerosols and cloud particles throughout the atmospheric column during the evolution of multiple deep convective storm systems. Coupling these new mea-**

**surements with detailed cloud simulations that resolve the size distributions of aerosols and cloud particles, we find several lines of evidence that most anvil crystals form on mid-tropospheric rather than boundary layer aerosols. This result defies conventional wisdom and indicates that distant pollution sources may impact anvil clouds more than local sources.**

It is well understood that cloud drops form on existing atmospheric aerosols, such as sulfuric acid particles and dust. Thus, changes in aerosol number can lead to changes in drop number during cloud formation. Complex subsequent effects on cloud microphysical development vary, depending upon cloud type and environmental conditions (*1*). The overall impact of increasing anthropogenic aerosols on low clouds such as stratocumulus may be great, generally resulting in smaller, more numerous drops and leading to brighter, longer-lived clouds that reflect more sunlight (*2, 3*). Since stratocumulus persistently cover large global areas, it has been recognized that this aerosol-induced cooling effect partially offsets the warming effect of accumulating greenhouse gas concentrations (*4*).

Whereas low clouds such as stratocumulus alter the global solar radiative budget with little influence on the infrared budget, high clouds such as cirrus reduce both solar incoming and infrared outgoing radiative fluxes by comparable amounts. Whether the overall impact is warming or cooling depends in a sensitive manner upon cloud optical depth and ice crystal effective radius (*5*), among other factors. While cirrus have a much lesser influence on the net radiative budget per unit area than stratocumulus, tropical anvil coverage may respond strongly to increasing sea surface temperatures, thereby playing a major role in global climate sensitivity (*6–8*). However, the properties and evolution of anvil cirrus remain poorly understood and weakly constrained in models (*9*). Recent observations also suggest that tropical cloud coverage may be rapidly changing in a manner not captured by current general circulation model simulations (*10*), which further motivates a better understanding of anvil-forming cumulonimbus clouds.

The Cirrus Regional Study of Tropical Anvils and Cirrus Layers– Florida Area Cirrus Experiment (CRYSTAL–FACE) was coordinated by the National Aeronautical and Space Administration (NASA) with the primary goal of fully characterizing subtropical cumulonimbus anvil formation and evolution. The experiment took place throughout July 2002 over southern Florida, where simultaneous measurements were made from six aircraft and three ground stations, as well as satellite platforms, over the lifetimes of many storm systems. Data gathered include simultaneous measurements of the number and size distribution of aerosols and cloud particles throughout the full depth of developing cumulonimbus columns. While a handful of previous modeling studies and data analyses have addressed the potential impact of boundary layer aerosol loading on the microphysical properties of clouds associated with deep convection (*11–14*), here we incorporate these extensive new measurements into a detailed three-dimensional modeling analysis with appropriate vertical variation of the aerosol field.

An unexpected result of this study is our finding that the fundamental source of nuclei on which most anvil crystals initially form is the mid-troposphere at 6–10 km rather than the planetary boundary layer near the Earth's surface (*13*). Several lines of evidence for this conclusion emanate from a case study of the highest-strength updraft ($>$20 m s$^{-1}$) that was penetrated directly by aircraft during the CRYSTAL–FACE campaign, on July 18. Since most cloud particles are formed where supersaturations reach peak values (*15*), in high-strength updraft cores, these measurements provide a unique window into the microphysical environment governing the injection of cloud particles into anvil cirrus. While CRYSTAL–FACE conditions do not include deep convection in the presence of heavy smoke or active fires (*14*), they are representative of subtropical continental deep convection.

On July 18, the University of North Dakota Citation aircraft measured aerosols and cloud particles at 7–12 km along the developing sea breeze fronts and penetrated the high-

strength updraft east of Lake Okeechobee at approximately 10 km in altitude (Fig. 1). The Center for Interdisciplinary Remotely-Piloted Aircraft Studies (CIRPAS) Twin Otter aircraft meanwhile measured aerosols and cloud particles between the surface and 4 km over the southwest Florida peninsula. NASA's WB-57 aircraft, which generally measured aerosols and cloud particles at 12–16 km, did not operate on July 18, but we are able to use WB-57 aerosol and cloud observations collected under similar conditions on other days to complement this case study. We thus incorporate observations from all three aircraft making in situ measurements during CRYSTAL-FACE (*16*).

To simulate the development of high-strength updrafts similar to the one observed, we use three-dimensional, large-eddy simulations with size-resolved microphysics (*16–19*). We initialize the model domain with a meteorological profile derived from local rawinsonde measurements (*16*) and an aerosol profile (Table 1) derived from aircraft measurements (*16*). Surface heat and moisture fluxes are assimilated from mesoscale weather model predictions for July 18 (*16, 20*) at the location of observed convection. The model transports aerosols, liquid drops, and ice particles, and accounts for activation, condensational growth, evaporation, sedimentation, and melting (*21*); gravitational collection (*21–23*); spontaneous and collision-induced drop breakup (*22, 24*); homogeneous and heterogeneous freezing of aerosols and drops (*21, 25*); and Hallett-Mossop rime splintering (*21*). Simulations exhibit chaotic generation of mature, high-strength updrafts throughout the last two hours of each three-hour simulation. We then compare simulated cloud particle properties in similar-strength updrafts with measurements made in the updraft on July 18 and in typical thick anvil cloud on July 21.

Turning first to measurements made in the updraft core on July 18 at 10 km altitude, we find that including tropospheric aerosols above 6 km is required to accurately simulate the large number of cloud particles observed in the updraft core at 10 km (Fig. 2). Aerosols below 2 km, which well exceeds the typical 1-km boundary layer height, are grossly insuffi-

cient to account for the observed numbers of cloud particles. Aerosols below 6 km are also insufficient, but when all aerosols up to the 10 km updraft penetration altitude are included in the simulation, the number of cloud particles as a function of vertical wind speed closely matches the observations. Furthermore, in both simulations and measurements, peak particle numbers are found not at peak updraft speeds, where peak supersaturations are located, but instead are found at intermediate updraft speeds (Fig. 2A). This pattern, coupled with the importance of entrained mid-tropospheric aerosols to reproducing the observed cloud particle number concentrations, suggests that the highest particle numbers are found in an entraining region of the updraft core. In the entrainment region, turbulent mixing laterally brings in mid-tropospheric aerosols, which are exposed to higher supersaturations, activated, and then carried aloft.

A second line of evidence derives from a closer examination of the measured variation of cloud particle size distribution during the updraft traversal, which was flown horizontally from downwind to upwind. Choosing a similar path through a simulated updraft core and comparing it with these measurements, both measurements and simulation results show that peak number is reached upwind of peak vertical wind speed as the core is traversed (Figs. 3A and 3B). This region where particle numbers reach their peak values is also characterized by a mixture of source air (Figs. 3C and 3D), indicative of significant entrainment. In both simulations and observations, we further find that the additional cloud particles in this upwind entraining region are much smaller than those in the heart of the core (Figs. 3E and 3F), which is the pattern that would be expected in the case of activation on recently entrained free-tropospheric aerosols.

Finally we consider whether simulated cloud particle number and size match observations in the upper anvil, where high-strength updraft cores detrain. While the upper-level anvil was not sampled on July 18, anvils from similar small cumulonimbus systems were sampled on July 11, 16, 19, 21, and 28. Using observations in a typical thick anvil be-

tween 12 and 14 km on July 21 as an example (other days appear similar), the measurements consistently indicate peak crystal number concentrations in the 20–30 $\mu$m diameter range. Model simulations on July 18 reproduce this peak accurately and consistently when aerosols are included throughout the atmospheric column, but the peak shifts to 50–60 $\mu$m when aerosols above 6 km are excluded, and shifts to even larger sizes when aerosols above 2 km are excluded (Fig. 4). These comparisons in the upper-level anvil support our analysis of the updraft measurements, providing a third line of evidence for the importance of mid-tropospheric aerosols. Since peak size is negligibly affected when aerosols above 10 km are excluded, those do not appear to be an important source of anvil nuclei. We estimate that the aerosols entrained between 6 and 10 km account for approximately two-thirds of the anvil nuclei (Fig. 4B versus 4C). We obtain similar results in simulations of convective events on other days during CRYSTAL–FACE, despite varying updraft strength and thermodynamic conditions.

It is initially surprising to find that mid-tropospheric aerosols determine fundamental anvil properties, because deep convection updraft cores are generally assumed to be relatively undilute parcels that travel from cloud base to cloud anvil with little entrainment (*13*). However, this assumption has recently been challenged by Zipser (*26*), who makes a distinction between relatively undilute, high velocity, mid-latitude supercell updrafts and highly dilute, lower-velocity, tropical marine updrafts. The updrafts observed during CRYSTAL–FACE appear to lie along this continuum, with intermediate vertical wind speed and dilution. Analysis of laboratory thermals indicates that entrainment scales inversely with updraft diameter, and when the toroidal rotation of rising updrafts is considered, also provides the rule of thumb that an updraft is turned "inside out" once over a vertical distance that matches the updraft diameter (*15*). Whereas the updraft cores of mid-latitude supercells may be 18 km in diameter (*27*), corresponding to less than a full toroidal rotation during ascent to the tropopause, the Florida updraft observed on July 18 exhibited

an updraft diameter of less than 5 km, corresponding to at least two such rotations. These order-of-magnitude estimates support the importance of mid-tropospheric entrainment.

There are important implications of our finding that anvil crystal number and size are determined by the entrainment of mid-tropospheric aerosols. Crystal size itself is a leading factor controlling cirrus radiative properties, with smaller crystals corresponding to higher cloud albedo (*5*). Owing to the apparently widespread presence of small anvil crystals in recent measurements, Garrett et al. (*28*) argue that there may be a need for substantial corrections to parameterizations of cirrus clouds in global climate models. It has also been suggested that the size of anvil ice crystals may control relative humidity near the tropopause, and by extension, moisture transport into the lower stratosphere (*29, 30*). By attributing anvil crystal formation to entrained mid-tropospheric aerosols (Fig. 4), we also provide a new explanation for the generation of copious small crystals that have been reported at anvil tops (*31*). The source of such crystals has been a puzzle, and they have been previously attributed to aerosol activation either at cloud top (*31*) or at cloud base (*11*).

Further implications hinge on our corollary finding that extreme variations in boundary layer aerosol concentrations, from polluted to clean conditions, influence anvil properties less than do mid-tropospheric aerosol concentrations (Figs. 2E and 2F). Thus, the documented long-range transport of pollution in the middle and upper troposphere (*32*) may be widely impacting cirrus radiative properties, evolution, and lifetime. But the details of such impacts are not obvious. Recent surveys of aerosol number and size derived from multiple field experiments over tropical and subtropical regions demonstrate that there are often more than twice as many aerosols present in clean mid-tropospheric air at 6–10 km than in polluted air (*33*) and that aerosol number at 8–12 km is highest when the atmosphere is devoid of nonvolatile pollution aerosols (*34*). Thus, pollution and aerosol number, which are closely correlated in the boundary layer, are frequently anti-correlated in the upper troposphere, perhaps owing to the scavenging of aerosol nucleation precursor gases by existing

pollution aerosol surface area (*34*). It is thus possible that more polluted environments would yield fewer, larger anvil crystals than cleaner environments, in direct contrast to the aforementioned case of marine stratocumulus, wherein polluted environments yield more, smaller cloud particles. Since supersaturations may reach high values in cumulonimbus updrafts (*22*) and aerosol activation is therefore sensitive to cloud dynamics, a detailed analysis of aerosol size distributions and geographic variations in cloud dynamics is required to establish the overall effect of pollution on anvil cirrus. Our analysis nonetheless indicates that long-range transport of pollution can dominate the effect of local sources on subtropical anvils.

## References and Notes


1. H. Graf, *Science* **303**, 1309 (2004).

2. S. Twomey, *Atmos. Environ.* **8**, 1251 (1974).

3. B. A. Albrecht, *Science* **245**, 1227 (1989).

4. Intergovernmental Panel on Climate Change, *Climate Change 2001: The Scientific Basis* (Cambridge University Press, 2001). (J. T. Houghton, Y. Ding, D. J. Griggs, M. Noguer, P. J. van der Linden, X. Dai, K. Maskell, and C. A. Johnson, Eds.).

5. G. L. Stephens, S.-C. Tsay, P. W. Stackhouse, Jr., P. J. Flatau, *J. Atmos. Sci.* **47**, 1742 (1990).

6. V. Ramanathan, W. Collins, *Nature* **351**, 27 (1991).

7. U. Lohmann, E. Roeckner, *J. Geophys. Res.* **100**, 16,305 (1995).

8. R. S. Lindzen, M.-D. Chou, A. Y. Hou, *Bull. Amer. Meteor. Soc.* **82**, 417 (2001).

9. A. D. Del Genio, W. Kovari, *J. Climate* **15**, 2597 (2002).

10. B. A. Wielicki, *et al.*, *Science* **295**, 841 (2002).

11. A. P. Khain, D. Rosenfeld, A. Pokrovsky, *Geophys. Res. Lett.* **28**, 3887 (2001).

12. V. T. J. Phillips, T. W. Choularton, A. M. Blyth, J. Latham, *Quart. J. Roy. Meteor. Soc.* **128**, 951 (2002).

13. S. C. Sherwood, *J. Climate* **15**, 1051 (2002).

14. M. O. Andreae, *et al.*, *Science* **303**, 1337 (2004).

15. R. A. Houze, Jr., *Cloud Dynamics* (Academic Press, 1977).

16. Materials and methods are available as supporting material on *Science* Online.

17. D. E. Stevens, A. S. Ackerman, C. S. Bretherton, *J. Atmos. Sci.* **59**, 3285 (2002).

18. E. J. Jensen, L. Pfister, A. S. Ackerman, O. B. Toon, A. Tabazadeh, *J. Geophys. Res.* **106**, 17,237 (2001).

19. A. S. Ackerman, O. B. Toon, D. E. Stevens, J. A. Coakley, Jr., *Geophys. Res. Lett.* **30**, 10.1029/2002GL016634 (2003).

20. M. Xue, D.-H. Wang, J.-D. Gao, K. Brewster, K. K. Droegemeier, *Meteor. Atmos. Phys.* **82**, 139 (2003).

21. H. R. Pruppacher, J. D. Klett, *Microphysics of Clouds and Precipitation* (Kluwer Academic Publishers, 1997).

22. W. D. Hall, *J. Atmos. Sci.* **37**, 2486 (1980).

23. M. Z. Jacobson, R. P. Turco, E. J. Jensen, O. B. Toon, *Atmos. Environ.* **28A**, 1327 (1994).

24. R. List, N. R. Donaldson, R. E. Stewart, *J. Atmos. Sci.* **44**, 362 (1987).

25. H. P. Meyers, P. J. DeMott, W. R. Cotton, *J. Appl. Meteor.* **31**, 708 (1992).

26. E. J. Zipser, *Cloud Systems, Hurricanes, and the Tropical Rainfall Measuring Mission (TRMM)*, W.-K. Tao, R. Adler, eds. (American Meteorological Society, 2003), vol. 29 of *Meteorological Monographs*, chap. 5, pp. 49–58.

27. D. J. Musil, A. J. Heymsfield, P. L. Smith, *J. Climate Appl. Met.* **25**, 1037 (1986).

28. T. J. Garrett, H. Gerber, D. G. Baumgardner, C. H. Twohy, E. M. Weinstock, *Geophys. Res. Lett.* **30**, 10.1029/2003GL018153 (2003).

29. S. C. Sherwood, *Science* **295**, 1272 (2002).

30. P. K. Wang, *J. Geophys. Res.* **108**, 10.1029/2002JD002581 (2003).

31. R. G. Knollenberg, K. Kelly, J. C. Wilson, *J. Geophys. Res.* **98**, 8639 (1993).

32. J. Lelieveld, *et al.*, *Science* **298**, 794 (2002).

33. A. D. Clarke, V. N. Kapustin, *J. Atmos. Sci.* **59**, 363 (2002).

34. H. B. Singh, *et al.*, *J. Geophys. Res.* **107**, 10.1029/2001JD000486 (2002).

35. We thank Jamison Smith and Brian Toon for raising questions about the relative importance of boundary layer and free tropospheric aerosols, Edward Zipser for sharing his extensive experience with tropical convection, William McKie for keeping our 70+ computers running in concert from Key West to Mountain View, and Donald Anderson for leading CRYSTAL–FACE with long-term vision. All of the data collection and modeling associated with this work was coordinated by NASA's Earth Science Enterprise through NRA-01-OES-02, with funding and support provided by NASA, the National Oceanic and Atmospheric Administration, the National Science Foundation, the Department of Energy (DOE), the Office of Naval Research, and the United States

Weather Research Program. We gratefully acknowledge additional computing support provided by DOE's High Performance Computing Facility.

**Supporting Online Material**

www.sciencemag.org

Materials and Methods

References

Table 1: Aerosol profile number and log-normal size distribution parameters

| Elevation (km) | Number ($cm^{-3}$) | Mode diameter ($\mu$m) | Standard deviation (-) |
|---|---|---|---|
| Baseline | | | |
| 15[a] | 100 | 0.025 | 1.6 |
| 10[b] | 3000 | 0.025 | 1.6 |
| 5[c] | 1200 | 0.025 | 1.6 |
| 2[d] | 1200 | 0.05 | 2.5 |
| <1[e] | 1800 | 0.11 | 1.9 |
| Clean | | | |
| <1[f] | 400 | | |
| | 275 | 0.035 | 1.5 |
| | 125 | 0.11 | 1.4 |
| Polluted | | | |
| <1[g] | 6500 | | |
| | 3000 | 0.03 | 1.5 |
| | 3500 | 0.12 | 1.8 |

[a] Since no WB-57 aircraft measurements are available for July 18, typical number and size distribution parameters for the uppermost troposphere are derived from measurements made on July 19.

[b] The number concentration of aerosols at 10 km is set to the number measured by the Citation aircraft upon entering the updraft-containing cloud. Since no size distribution measurements are available for the Citation, typical size distribution parameters measured by the WB-57 on July 19 are assumed.

[c] The number concentration of aerosols at 5 km is set to the typical number measured by the Citation on July 18 at that elevation. Size distribution parameters as aloft.

[d] The number concentration of aerosols at 2 km is set to the typical number measured by both Citation and Twin Otter aircraft on July 18 at that elevation. Size distribution parameters are derived from Twin Otter measurements made in the vicinity of that number concentration and elevation on July 18.

[e] All July 18 Twin Otter measurements were made over the southwest peninsula, downwind of continental and pollution sources, whereas the high-strength updraft formed at the east coast in onshore winds. Baseline number concentration and size distribution are therefore derived from the cleanest boundary layer aerosols sampled by the Twin Otter on July 18.

[f] Sensitivity test parameters derived from Twin Otter measurements of clean marine boundary layer aerosols sampled on July 25, which were markedly bimodal and are therefore represented as the sum of the two modes listed. No such clean conditions were encountered on July 18.

[g] Sensitivity test parameters derived from measurements of polluted boundary layer aerosols sampled on July 18, which were also strongly bimodal.

Fig. 1. Flight track of the Citation aircraft through the developing updraft core on July 18, directly east of Lake Okeechobee. The experiment-wide peak updraft speed of approximately 23 m $s^{-1}$ was measured at 17:49:10 UTC, four minutes after the underlying satellite image was taken. Figure courtesy of Patrick Minnis and Louis Nguyen, NASA Langley Research Center.

Fig. 2. Cloud particle number versus vertical wind speed measured near 10 km altitude in the updraft core (red) and simulated in the nearest layers above and below 10 km (blue and green) when simulated peak vertical wind speeds are similar to those observed. Model results show closest agreement with observations when all aerosols are included in the simulation (A). Agreement degrades when free tropospheric aerosols are excluded above 8 km (B), 6 km (C), and 2 km (D), and is less sensitive to replacing moderate aerosol concentrations of 1800 $cm^{-3}$ in the boundary layer with clean marine aerosol of 400 $cm^{-3}$ (E) or polluted aerosol of 6500 $cm^{-3}$ (F). See Table 1 for aerosol number size distribution parameters.

Fig. 3. Comparison of 2-s average measurements across the updraft (A) with results along a 4-km path through a similar-strength updraft in the baseline simulation (B). Updraft strength (triangles) and cloud particle number concentration (diamonds) are denoted by color in three regions: downwind in the core (blue), within the entrainment region (green), and upwind of the core (red). Equivalent potential temperatures, normalized by their respective measured and simulated ranges, demonstrate that the green points occupy an entrainment region of both the measured updraft (C) and the simulated updraft (D). Cloud particle size distributions show that the entrainment region is characterized by increased numbers of the smallest particles in both measurements (E) and simulation results (F). The simulated core is generally wider and more uniform than the observed core at least in

part because of limitations on model resolution (*16*).

Fig. 4. A cross-section of simulated cloud particle number concentration with a black diamond at the 13-km location of highest predicted number (A), and the ice crystal size distributions (B) simulated at that location (black line) and measured at 12–14 km on July 21 (colored lines). Simulated peak diameters closely match measured peak diameters at 20–30 $\mu$m when all aerosols are included (A and B), but shift to larger sizes, exhibiting successively poorer agreement with the measurements, when aerosols are excluded above 6 km (C and D) and above 2 km (E and F),

Fig. 1

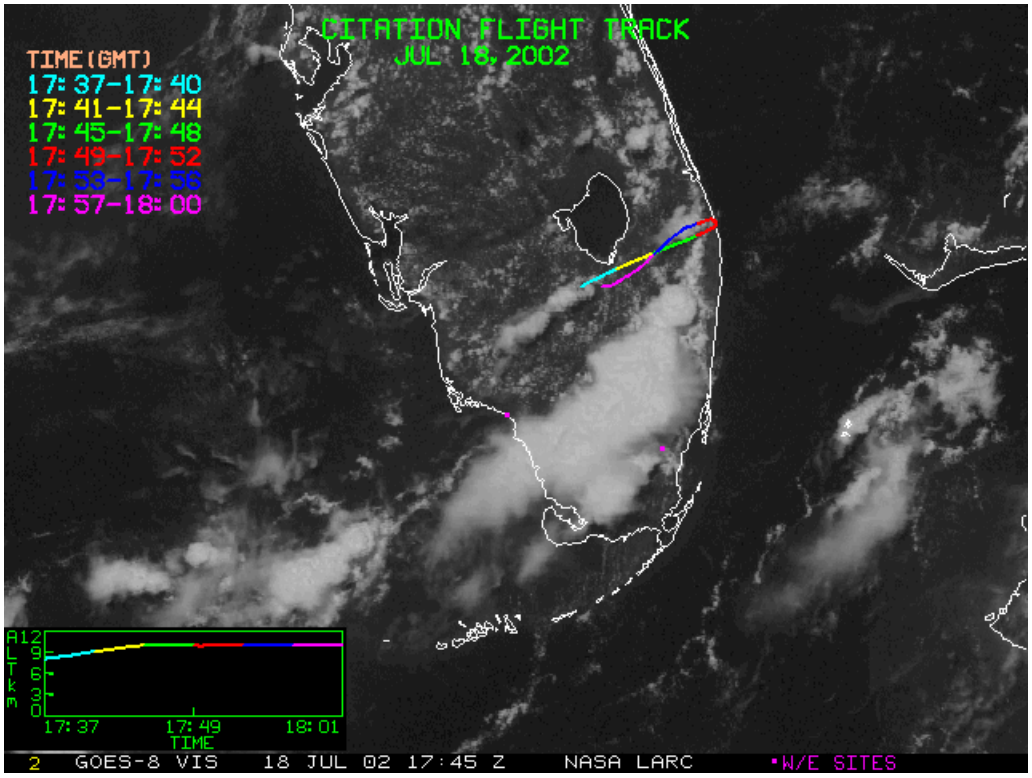
CITATION FLIGHT TRACK
JUL 18, 2002
TIME(GMT)
17:37-17:40
17:41-17:44
17:45-17:48
17:49-17:52
17:53-17:56
17:57-18:00
ALT km
12
9
6
3
0
17:37
17:49
18:01
TIME
2 GOES-8 VIS 18 JUL 02 17:45 Z NASA LARC •W/E SITES

Fig. 2

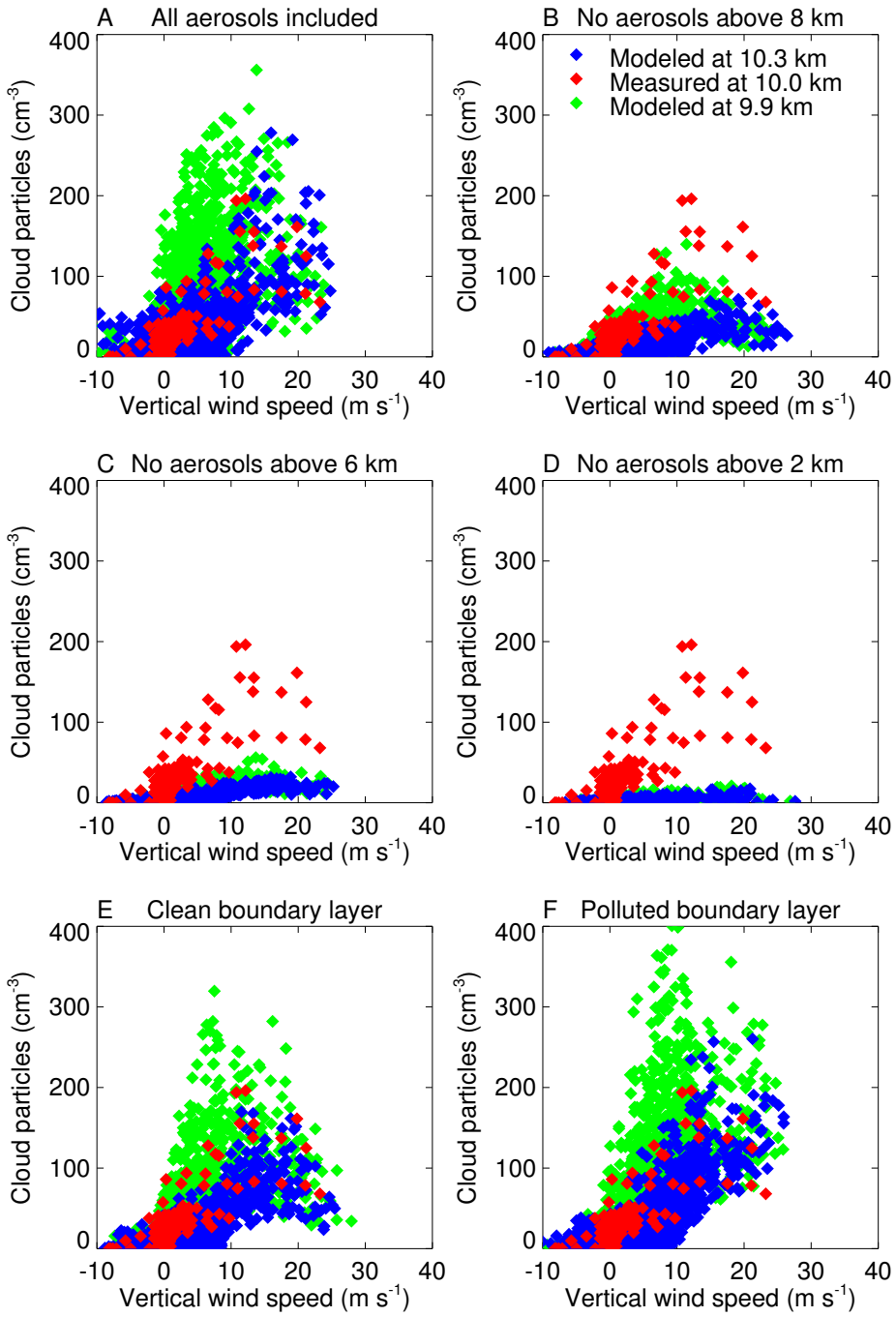
A All aerosols included
B No aerosols above 8 km
Modeled at 10.3 km
Measured at 10.0 km
Modeled at 9.9 km
C No aerosols above 6 km
D No aerosols above 2 km
E Clean boundary layer
F Polluted boundary layer
Cloud particles (cm-3)
Vertical wind speed (m s-1)
0
100
200
300
400
-10
0
10
20
30
40

Fig. 3

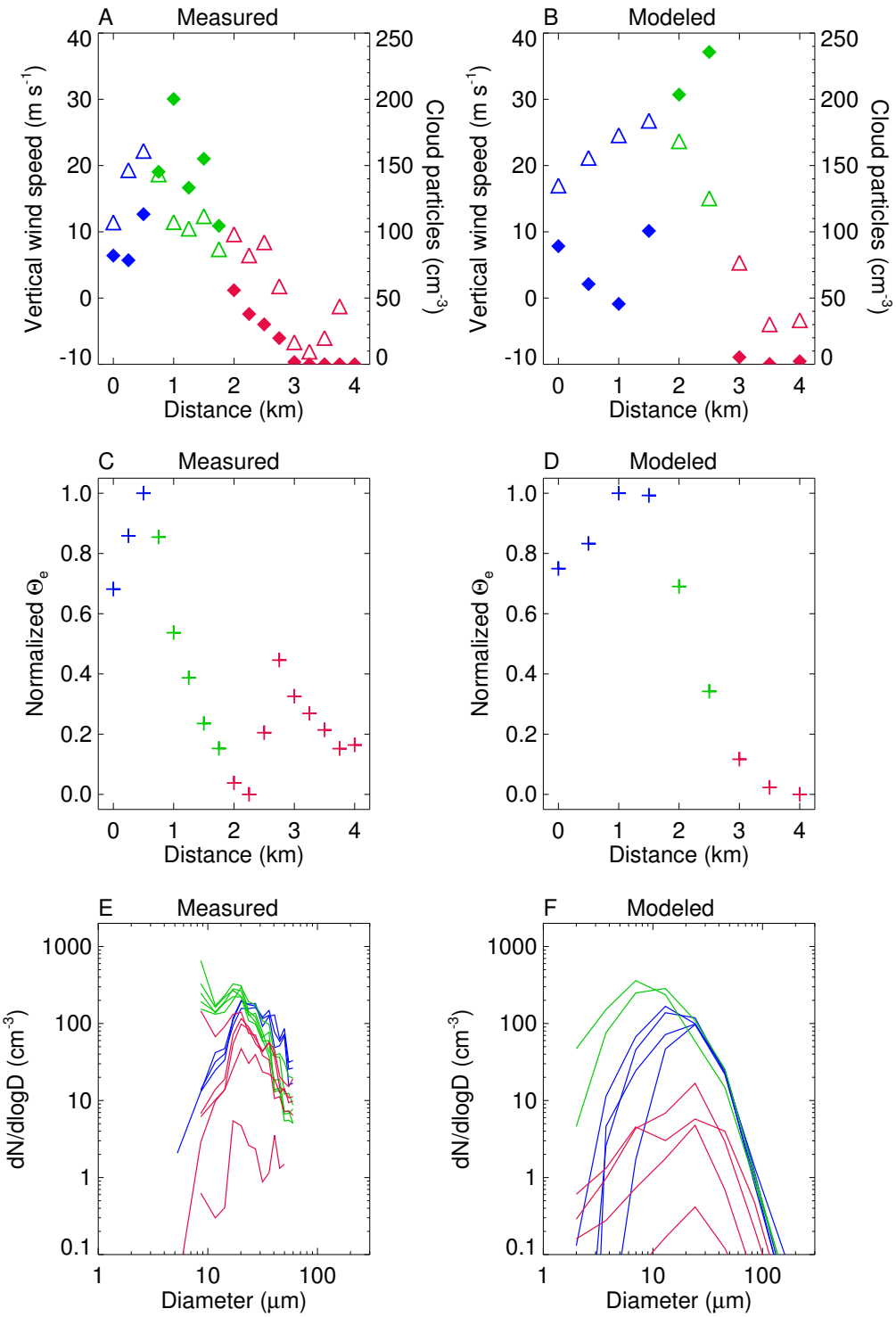
A
Measured
B
Modeled
Vertical wind speed (m s-1)
Cloud particles (cm-3)
Distance (km)
C
Measured
D
Modeled
Normalized Θe
E
Measured
F
Modeled
dN/dlogD (cm-3)
Diameter (μm)

Fig. 4

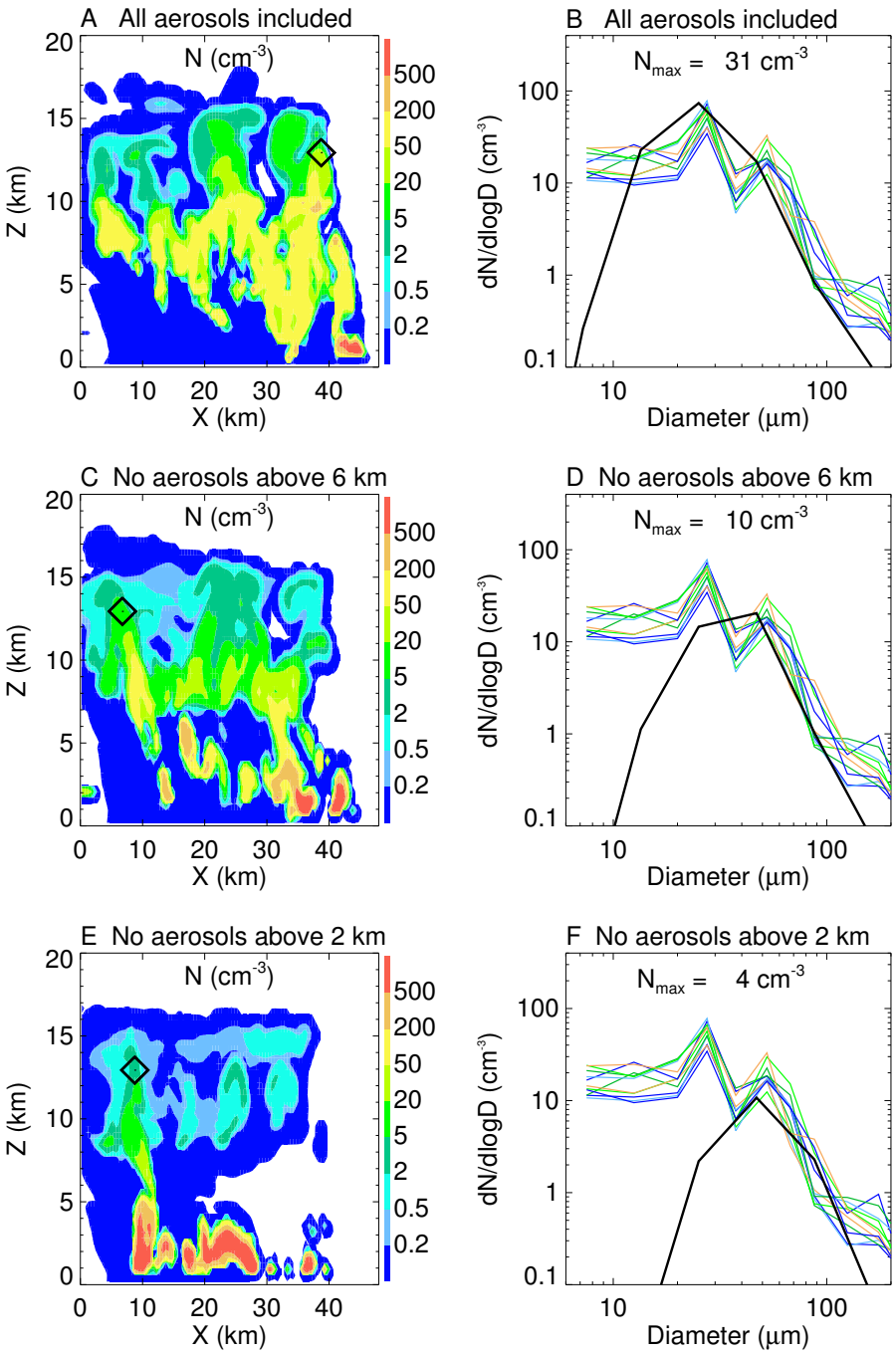
A All aerosols included
N (cm-3)
Z (km)
X (km)
B All aerosols included
Nmax = 31 cm-3
dN/dlogD (cm-3)
Diameter (μm)
C No aerosols above 6 km
D No aerosols above 6 km
Nmax = 10 cm-3
E No aerosols above 2 km
F No aerosols above 2 km
Nmax = 4 cm-3

# Supporting online material

## Materials and methods

### Model description

We use a 48-km square horizontal by 24-km vertical domain with uniform 500-m horizontal by 375-m vertical grid spacing. A dynamics model (*S1*) integrates the anelastic equations for deep convection (*S2*) in conservative form using a 5-s time step, a third-order advection scheme, a standard Smagorinsky subgrid parameterization, and a sponge layer above 20 km. Boundary conditions are rigid at the top and bottom and open at the horizontal faces, where a cosine-squared forcing function is used to nudge values to the initial conditions in a 4.5-km swath along each face. In lieu of a soil model, we assimilate surface heat and moisture fluxes from forecasts of NASA Langley's Advanced Regional Prediction System (ARPS) mesoscale model (*S3*) initialized at 12:00 UTC on July 18. Starting at 16:00 UTC in the domain of the observed updraft, we spatially and temporally interpolate ARPS output from 15-km and 30-min resolution to our 500-m and 5-s resolution.

An embedded microphysics model (*S4, S5*) discretizes the size distributions of aerosols, drops, and ice particles into 16 mass bins each, spanning diameters of 5 nm–1 $\mu$m, 2 $\mu$m–1 cm, and 2 $\mu$m–>3 cm, respectively. Drop density is set to 1.0 g cm$^{-3}$ and ice density is set to 0.9 g cm$^{-3}$ below 300 $\mu$m in diameter, above which it decreases according to observations for lump graupel (*S6*). Height-dependent fall velocities are calculated as a function of particle mass and size according to Reynolds number regime, assuming spherical particles of deformable liquid or rigid, rough ice (*S7*). Fall velocities are combined

with radius-dependent collision efficiencies (*S8*) to derive a height-dependent gravitational collection kernel that is integrated semi-implicitly (*S9*). Drops coagulating with ice are assumed to freeze instantaneously. Additional kernels for spontaneous and collision-induced drop breakup (*S8, S10*) are integrated explicitly, but the effect of turbulence on coagulation is currently neglected. Gravitational collection and drop breakup are the only microphysical processes always advanced with the 5-s dynamical time step, whereas all other microphysical processes are advanced with a time step that varies to a minimum value of 0.2 s.

We have extended previous modeling studies of continental deep convection (*S11, S12*) by using aerosol size distributions based on measurements throughout the boundary layer and free troposphere, calculating supersaturations required for activation (*S7*), removing aerosols from the size distribution as they are activated, and allowing for three-dimensional transport. By contrast, the previous studies use a power-law formulation to estimate the number of aerosols activated, $N = Cs^k$, where $s$ is the supersaturation in percent and $C$ and $k$ are positive constants that do not vary. While numerically efficient, the power-law formulation provides an infinite source of aerosols with increasing supersaturation and does not distinguish between the properties of boundary layer and free tropospheric aerosols. These factors become important in our simulated updrafts because high supersaturations activate all of the initial boundary layer aerosols, leaving negligibly few except for those entrained from the free troposphere, which exhibit markedly different number size distributions. Our treatment does require a knowledge of aerosol chemical composition, which we assume to be ammonium bisulfate. Chemical composition is undoubtedly more complex, but an aerosol/cloud condensation nuclei closure study has shown that assuming ammonium bisulfate nonetheless can provide a remarkably accurate representation of activation during CRYSTAL-FACE (*S13*).

Homogeneous freezing of aerosols and drops is treated classically here (*S7*) and results

are insensitive to a newer parameterization (*S14*). Results are also insensitive to inclusion of heterogeneous freezing by low concentrations of ice nuclei (IN), which we relate to temperature, ice supersaturation, and the numbers of particles present as follows. IN are assumed to be present at a background concentration of 0.06 $cm^{-3}$, consistent with observations (*S15*) on July 18, and are assumed to be uniformly distributed among the total aerosols, drops, and ice particles in each grid cell. IN in drops are assumed to activate linearly with decreasing temperature over the range $-16$ to $-28°C$ (*S7*), whereas IN in aerosols are assumed to activate nonlinearly with increasing ice supersaturation (*S16*) over the range 4–32% at temperatures below $-5°C$. Based on the simplifying assumption that temperature decreases and supersaturation increases monotonically with increasing elevation in updrafts, the IN incrementally freeze aerosols and drops in a given grid cell if updraft velocity exceeds 5 m/s and an incremental temperature or supersaturation threshold is passed during traversal from the grid cell below. Overall, homogeneous freezing of drops contributes the majority of ice crystals in our simulations, although all other freezing mechanisms also contribute small numbers. This result appears reasonable in light of the low ratio of IN to peak anvil ice crystal numbers and the general agreement between simulated and observed particle numbers and size distributions.

All cloud-resolving model results are dependent upon parameterizations, such as the ones just described for ice formation, as well as spatial resolution. Our spatial resolution is determined by the requirement of sufficient domain size to contain growth of a realistic cluster of updrafts, on the one hand, and the requirement of sufficient computational memory, on the other hand. Previous modeling of shallow cumulus with bulk microphysics has demonstrated that some aspects of cloud simulations can be extremely difficult to converge with respect to increasing spatial resolution (*S1*). Using limited available time on 512 processors of the Department of Energy's National Energy Research Scientific Computing Center IBM SP RS/6000, we find that no aspect of our analysis here is affected by

a doubling of either spatial resolution or bin number. These sensitivity tests reach the bin resolution of recent two-dimensional simulations of deep convection that focus on tracking more particle types (*S11*) and exceed the spatial resolution of recent three-dimensional simulations of deep convection with bulk microphysics (*S17*). However, some aspects of our simulations, such as the width and complexity of updraft features, could become more realistic with increasing resolution (Fig. 3, as noted).

**Meteorological and aerosol measurements**

Using open lateral boundary conditions, all faces of the model domain are nudged to the initial meteorological and aerosol profiles throughout the simulation. We derive a single representative meteorological profile from rawinsonde measurements on July 18 at the Miami airport, located approximately 100 km south of the observed updraft and at a similar distance from the coastline. We use soundings measured at 14:35 UTC and 17:36 UTC with a Vaisala 80H sensor, corrected for known sensor time-lag and bias errors. Thermodynamic data from the later sounding, taken 13 minutes prior to the updraft penetration, were fouled by sensor icing from supercooled liquid water. However, wind data from the earlier sounding were poorly sampled over extreme speed changes at crucial mid-tropospheric elevations. We thus combine thermodynamic variables from the earlier sounding with winds from the later sounding.

We derive initial representative aerosol profiles for the baseline simulation and sensitivity tests (Table 1) from measurements made on three aircraft. From the Twin Otter aircraft data (below 4 km), we estimate aerosol number $> 10$ nm from sequential condensation particle counter (CPC) measurements of aerosols $> 7$ and 12 nm in diameter and we estimate aerosol size distribution from simultaneous differential mobility analyzer measurements reported in 100 size bins spanning 10 nm–1 $\mu$m in diameter. From the Citation aircraft data (5–12 km), we estimate aerosol number from CPC measurements of aerosols $> 10$ nm in diameter (aerosol size distribution was not measured on the Citation). From the WB-57

aircraft data (12–16 km), we estimate both aerosol number $> 10$ nm and size distribution from sequential nucleation mode aerosol size spectrometer (NMASS-II) measurements of aerosols $> 4$, 8, 15, 30, and 64 nm in diameter. Since no WB-57 measurements are available from July 18, we use measurements from July 19 to estimate the fall-off of aerosol number with elevation above 10 km and the size distribution of aerosols above 5 km.

While we benefit from a broad analysis of aerosol number and size distribution throughout the CRYSTAL-FACE experiment, precise aerosol conditions in and around the July 18 updraft remain uncertain since aerosol size distribution was not measured by the Citation, the WB-57 made no such measurements on July 18, and some of the Citation's in-cloud aerosol number measurements appear suspect. Aerosol number $> 10$ nm measured out-of-cloud is approximately 3000 and 4500 $cm^{-3}$ upon entry into and exit from the case study cloud, respectively. Aerosol number measured in-cloud also remains persistently high, never dropping below 1800 $cm^{-3}$ throughout the strong updraft. However, the extreme variability of numbers measured in the updraft is indicative of known CPC instrument errors in the presence of liquid water (*S18*), so we do not consider that data to be reliable. Thus, we focus here on the out-of-cloud aerosol measurements, with acknowledged uncertainty in their size distribution. For simplicity, we use typical monomodal parameters derived from size distributions measured by the WB-57 on July 19 in the absence of nucleation-mode particles and we arbitrarily use the entry value in our baseline profile at 10 km (Table 1). Our results are surprisingly insensitive to an increase of aerosol number up to the exit value using the monomodal parameters or using an additional mid-tropospheric nucleation mode, which can also explain some numbers remaining unactivated within the core.

**Cloud measurements**

Cloud particle size distributions measured on the Citation aircraft with a forward spectrometer scattering probe (FSSP-100) are reported as a function of maximum particle diameter in 15 bins spanning 4–62 $\mu$m. While FSSP measurements may be unreliable in the

presence of large ice crystals (*S19*), we find that integrations of the measured small particle size distributions match the volume of liquid water measured by both King and Rosemount icing probes. Cloud particle size distributions measured on the WB-57 aircraft with a cloud, aerosol, and precipitation spectrometer (CAPS) and an FSSP scattering spectrometer probe (SPP-100) are composited and reported as a function of maximum particle diameter in 25 bins spanning 0.35 $\mu$m–1.6 cm. Owing to the persistent presence of secondary peaks in particle concentration at diameters smaller than 6 $\mu$m and unexpected flattening of particle size distributions at diameters larger than 0.5 cm, we focus here on the central range of particle sizes between those limits (Fig. 4).

# References


S1. D. E. Stevens, A. S. Ackerman, C. S. Bretherton, *J. Atmos. Sci.* **59**, 3285 (2002).

S2. F. B. Lipps, R. S. Hemler, *J. Atmos. Sci.* **43**, 1796 (1986).

S3. M. Xue, D.-H. Wang, J.-D. Gao, K. Brewster, K. K. Droegemeier, *Meteor. Atmos. Phys.* **82**, 139 (2003).

S4. E. J. Jensen, L. Pfister, A. S. Ackerman, O. B. Toon, A. Tabazadeh, *J. Geophys. Res.* **106**, 17,237 (2001).

S5. A. S. Ackerman, O. B. Toon, D. E. Stevens, J. A. Coakley, Jr., *Geophys. Res. Lett.* **30**, 10.1029/2002GL016634 (2003).

S6. A. J. Heymsfield, P. N. Johnson, J. E. Dye, *J. Atmos. Sci.* **35**, 1689 (1978).

S7. H. R. Pruppacher, J. D. Klett, *Microphysics of Clouds and Precipitation* (Kluwer Academic Publishers, 1997).

S8. W. D. Hall, *J. Atmos. Sci.* **37**, 2486 (1980).

S9. M. Z. Jacobson, R. P. Turco, E. J. Jensen, O. B. Toon, *Atmos. Environ.* **28A**, 1327 (1994).

S10. R. List, N. R. Donaldson, R. E. Stewart, *J. Atmos. Sci.* **44**, 362 (1987).

S11. A. P. Khain, D. Rosenfeld, A. Pokrovsky, *Geophys. Res. Lett.* **28**, 3887 (2001).

S12. V. T. J. Phillips, T. W. Choularton, A. M. Blyth, J. Latham, *Quart. J. Roy. Meteor. Soc.* **128**, 951 (2002).

S13. T. M. VanReken, *et al.*, *J. Geophys. Res.* **108**, 10.1029/2003JD003582 (2003).

S14. T. Koop, B. Luo, A. Tsias, T. Peter, *Nature* **406**, 611 (2000).

S15. P. J. DeMott, *et al.*, *Geophys. Res. Lett.* **30**, 10.1029/2003GL017410 (2003).

S16. H. P. Meyers, P. J. DeMott, W. R. Cotton, *J. Appl. Meteor.* **31**, 708 (1992).

S17. P. K. Wang, *J. Geophys. Res.* **108**, 10.1029/2002JD002581 (2003).

S18. R. J. Weber, *et al.*, *J. Geophys. Res.* **103**, 28,337 (1998).

S19. J.-F. Gayet, G. Febvre, H. Larsen, *J. Atmos. Oceanic Technol.* **13**, 1300 (1996).